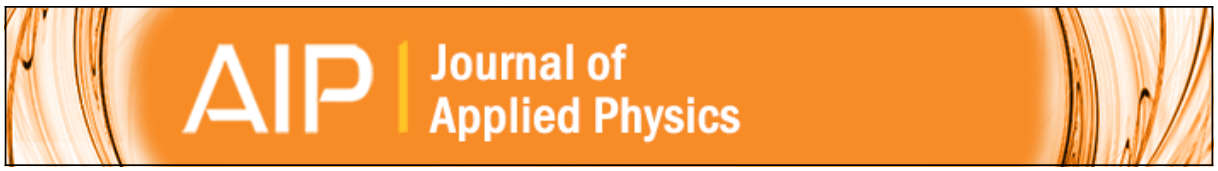

Nanometric particle size and phase controlled synthesis and characterization of γ-Fe2O3 or (α+γ)-Fe2O3 by a modified sol-gel method

Marcela F. Silva, Luiz A. S. de Oliveira, Mariani A. Ciciliati, Lais T. Silva, Bruna S. Pereira, Ana Adelina W. Hechenleitner, Daniela M. F. Oliveira, Kleber R. Pirota, Flávio F. Ivashita, Andrea Paesano Jr., J. Martin Pastor, J. Iñaki Pérez-Landazábal, and Edgardo A. G. Pineda

Citation: Journal of Applied Physics **114**, 104311 (2013); doi: 10.1063/1.4821253

View online: http://dx.doi.org/10.1063/1.4821253

View Table of Contents: http://scitation.aip.org/content/aip/journal/jap/114/10?ver=pdfcov

Published by the AIP Publishing

Nanometric particle size and phase controlled synthesis and characterization of γ-Fe_2O_3 or ($\alpha + \gamma$)-Fe_2O_3 by a modified sol-gel method

Marcela F. Silva,[1,a)] Luiz A. S. de Oliveira,[2] Mariani A. Ciciliati,[1] Lais T. Silva,[1] Bruna S. Pereira,[1] Ana Adelina W. Hechenleitner,[1] Daniela M. F. Oliveira,[1] Kleber R. Pirota,[2] Flávio F. Ivashita,[3] Andrea Paesano, Jr.,[3] J. Martin Pastor,[4] J. Iñaki Pérez-Landazábal,[4] and Edgardo A. G. Pineda[1]

[1]*Departamento de Química, Universidade Estadual de Maringá, 87020-900 Maringá-PR, Brazil*
[2]*Instituto de Física Gleb Wataghin, Universidade Estadual de Campinas, 13083-859 Campinas-SP, Brazil*
[3]*Departamento de Física, Universidade Estadual de Maringá, 87020-900 Maringá-PR, Brazil*
[4]*Departamento de Física, Universidad Pública de Navarra, Campus de Arrosadía, 31006 Pamplona, Spain*

(Received 5 July 2013; accepted 30 August 2013; published online 13 September 2013)

Fe_2O_3 nanoparticles with sizes ranging from 15 to 53 nm were synthesized by a modified sol-gel method. Maghemite particles as well as particles with admixture of maghemite and hematite were obtained and characterized by XRD, FTIR, UV-Vis photoacoustic and Mössbauer spectroscopy, TEM, and magnetic measurements. The size and hematite/maghemite ratio of the nanoparticles were controlled by changing the Fe:PVA (poly (vinyl alcohol)) monomeric unit ratio used in the medium reaction (1:6, 1:12, 1:18, and 1:24). The average size of the nanoparticles decreases, and the maghemite content increases with increasing PVA amount until 1:18 ratio. The maghemite and hematite nanoparticles showed cubic and hexagonal morphology, respectively. Direct band gap energy were 1.77 and 1.91 eV for A6 and A18 samples. Zero-field-cooling–field-cooling curves show that samples present superparamagnetic behavior. Maghemite-hematite phase transition and hematite Néel transition were observed near 700 K and 1015 K, respectively. Magnetization of the particles increases consistently with the increase in the amount of PVA used in the synthesis. Mössbauer spectra were adjusted with a hematite sextet and maghemite distribution for A6, A12, and A24 and with maghemite distribution for A18, in agreement with XRD results. © *2013 AIP Publishing LLC*. [http://dx.doi.org/10.1063/1.4821253]

I. INTRODUCTION

Iron oxides like magnetite (Fe_3O_4), maghemite (γ-Fe_2O_3), and hematite (α-Fe_2O_3) have been extensively investigated because of its magnetic, optical, and catalytic properties, as well as its low cost. They have been used as catalyst, adsorbents for organic or inorganic polluents,[1,2] as electrodes in batteries,[3] and for bioapplications.[4] In particular, magnetic iron oxides show interesting responses to external magnetic fields, which are suitable for clinical diagnosis, medical therapy,[5] and magnetic separation.[6] Generally, nano-sized materials exhibit novel physical and chemical properties, and consequently the synthesis of nanostructured iron oxides particles was intentionally studied.[7] Specific properties are also due to the huge specific area of nanoparticles enabling their dispersion within composites or giving a high surface reactivity for catalysts. The performances optimization of nanomaterials needs, however, a careful control of many characteristics (e.g., size, shape, crystalline structure for polymorph materials, dispersion state, surface state, etc.) on which their properties depend. In addition, it is desirable that the fabrication of nanomaterials has to be cheap, easy, and environmentally friendly.[8] Different methods have been applied to synthesize nanoparticles including thermal and hydrothermal techniques such as combustion,[9] sol–gel,[10,11] micro emulsion,[12] pyrolysis,[13] and even ultrasonic-assisted methods.[14] However, the most methods of iron oxide synthesis present disadvantages such as control of pH, moisture, and temperature of the medium, the use of expensive equipment, long time to obtain the materials, and the use of organic solvents, which are harmful to the environment.[8,15,16]

The present paper reports the synthesis of Fe_2O_3 nanoparticles using a relatively simple sol–gel method. Water was used as a solvent, and quick precipitation, combustion, and calcination were combined in only two steps. We previously reported the synthesis of NiO, $Ni_{0.04}Zn_{0.96}O$, $Fe_{0.03}Zn_{0.97}O$, ZnO, CuO, and a mixed Zn and Cu oxide by this method.[11,17] The goal of this paper is to study the influence of the amount of used polymer on the size, crystalline structure, and properties of the obtained material.

The synthesized nanoparticles were characterized by infrared spectroscopy (FTIR), X-ray powder diffractometry (XRD), transmission electron microscopy (TEM), magnetic measurements (magnetization versus temperature in the range of 5–1200 K and magnetization versus applied magnetic field), and Mössbauer spectroscopy.

II. EXPERIMENTAL METHODS AND MATERIALS

A. Materials

Ferric nitrate ($Fe(NO_3)_3 \cdot 9H_2O$) (Vetec, Brazil) and poly(vinyl alcohol) (PVA; MW 146 000-180 000 88%-89% hydrolyzed) (Aldrich, USA).

a)Author to whom correspondence should be addressed. Electronic mail: celafs@gmail.com

B. Synthesis

The iron oxide nanoparticles were synthesized by a modified sol-gel method.[11] Aqueous diluted PVA (10% w/v) and saturated ferric nitrate solutions were separately prepared and then mixed at Fe^{3+}:PVA monomeric unit ratios of 1:6, 1:12, 1:18, and 1:24, and the samples were, respectively, named as A6, A12, A18, and A24. The solutions were maintained at room temperature under stirring for 2 h and then heated under vigorous stirring until total water evaporation. The temperature was maintained at 150 °C for thermal degradation of the polymer. The nanostructured material was obtained after calcination of the material under air atmosphere at 400 °C for 4 h for elimination of residual organic materials from PVA.

C. Analysis

The iron oxide powders were characterized by infrared spectroscopy (FTIR) with an FTIR-BOMEM-100 Spectrometer using KBr pellets. The X-ray measurements were carried out on a Siemens D-5000 powder diffractometer with monochromated Cu-Kα radiation ($\lambda = 1.54056$ Å). Reflection X-ray powder diffraction data were collected from 10° to 90° in 2θ. Particle size was estimated using Scherrer's equation

$$d = \frac{0.9\lambda}{B\cos\theta}, \quad (1)$$

where λ is the wavelength, B the full width at half maximum (FWHM) of the peak, and θ the Bragg angle. The (220) diffraction peak of the maghemite and the (104) peak of the hematite were used for calculation of the average size particles for each phase. The Rietveld method and the Fullprof program[18] have been used to analyze the x-ray spectra.

The structures of the obtained iron oxides were analyzed with a 120 kV JEOL JEM-1400 TEM with a Carl Zeiss EM10 microscope with 80 kV. The samples were deposited on a pure carbon thin film Cu grid (with 200 mesh) (CF200-Cu, EMS).

The photoacoustic spectra were performed with a monochromatic light from a 1000 W xenon arc lamp—Oriel Corporation 68820, monochromator—model 77250, Oriel Instruments, mechanical chopper—Stanford Research Systems SR40.

The low temperature (5–300 K) magnetic measurements were performed in a Quantum Design MPMS XL-7 SQUID, whereas the room and higher temperatures were performed in a Lakeshore vibrating sample magnetometer (VSM – 2 T) equipped with an Ar flow furnace (300–1200 K).

Mössbauer spectra were taken from a constant acceleration spectrometer, with a ^{57}Co(Rh) source of 25 mCi of nominal starting activity. The Mössbauer spectra were analyzed using a non-linear least-square routine, with Lorentzian line shapes. Eventually, a hyperfine magnetic field distribution (Bhf) was used as histograms in the spectral analysis. All isomer shift (δ) data are given relative to α-Fe throughout this paper.

III. RESULTS AND DISCUSSION

The obtained iron oxides were analysed by FTIR spectroscopy, and the spectra are shown in Figure 1. These

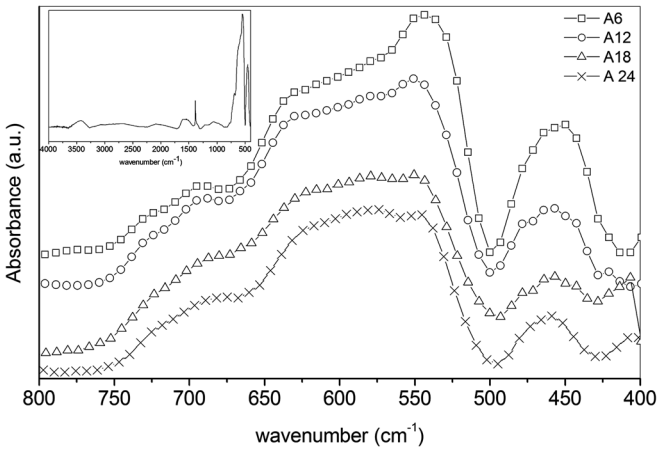

FIG. 1. FTIR spectra for obtained iron oxides, with zoom in the region of 800-400 cm^{-1}, showing the bands related with Fe-O vibrations. Inset: FTIR spectrum of A6 for the entire region of wavenumber.

spectra show only an alteration of one peak (540 cm^{-1}) intensity, indicating that the chemical composition of A6, A12, A18, and A24 are similar. Impurities arising either from the method of preparation or from adsorption of atmospheric compounds can produce distinct bands in the spectra of iron oxides (e.g., as at 1400 cm^{-1}, related to residual nitrate[19]). The IR bands at 3400 cm^{-1} and 1600 cm^{-1} can be assigned to OH stretching (ν OH) and HOH bending (δ OH) vibrational bands due to the adsorbed water in the sample.[20,21] The bands in the range of 750–400 cm^{-1} are related to Fe-O lattice vibration. Maghemite phase presents bands at 700, 660–630, 590, and 430 cm^{-1} and hematite phase presents bands at 540 and 470 cm^{-1}, but the positions of the bands are sensitive to particle size and shape.[19,22]

It can be observed that the intensity of the bands at 540 cm^{-1} (related to hematite phase) is higher than the bands at 590 and 630 cm^{-1} (related to maghemite phase) for A6 and A12 samples. However, for A18 and A24 samples, the intensities of these bands are the same. This behavior can be attributed to different particle size and shape and also to different phase composition of the samples, indicating higher hematite contents in A6 and A12.

To identify and quantify the iron oxides phases and to evaluate the size of each phase, x-ray diffractograms were measured. XRD-patterns of all samples are shown in Figure 2. The diffraction patterns are in perfect agreement with the standard JCPDS 39-1346 (maghemite) and JCPDS 87-1166 (hematite). The samples A6, A12, and A24 present peaks of the two indicated phases (hematite and maghemite) while sample A18 only shows peaks related to maghemite phase.

The quantitative data analysis of the crystalline phases (carried out by Rietveld refinement) and the particle sizes (determined by the Scherrer's equation) are presented in Table I.

It is observed that changing the molar ratio of the Fe^{3+}:PVA monomer from 1:6 to 1:18, there is a decrease in the peaks intensity of hematite phase and an increase in the peaks corresponding to maghemite phase. In the A18 sample diffractogram the hematite peaks are not visible, indicating that this phase in not present and that this sample consists only of the maghemite phase. When the Fe^{3+}:PVA unit

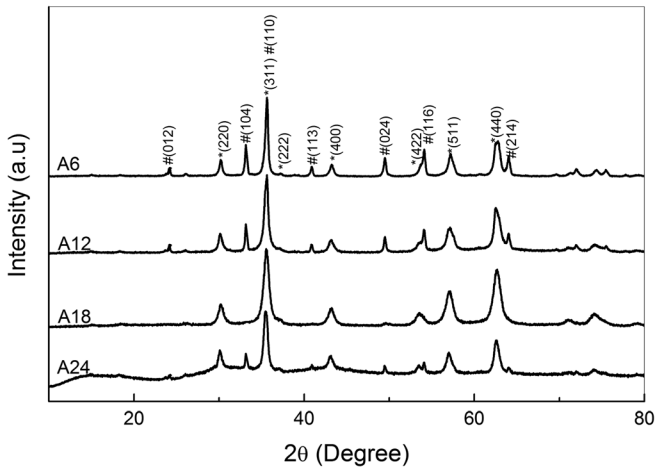

FIG. 2. XRD pattern of A6, A12, A18, and A24 samples. The Miller indices of reflection are assigned as * for maghemite and # for hematite.

monomer ratio is further increased to 1:24, the XRD analysis shows hematite and maghemite peaks again, suggesting that it is only possible to prepare maghemite using a specific metal:monomer ratio (near 1:18). Both hematite and maghemite nanoparticles average size show a decrease as the amount of polymer in relation to iron ions is increased (data showed in Table I).

The main polymer function in the reaction liquid medium is to provide a polymeric network to hinder cation mobility allowing local stoichiometry to be maintained and minimizing precipitation of unwanted phases. In aqueous PVA solutions, many metals can be stabilized at the polymer via interactions with OH groups.[23,24]

In opposition to results obtained in previous studies using PVA sol-gel method for the synthesis of metal oxides,[25,26] we observed that the PVA amount directly influences obtained particle size and crystalline phases. Further, PVA is believed to have selective interaction between different planes of iron oxide crystal, thus enhancing the growth of one specific phase. Therefore, with different PVA and iron salt concentrations, we can control the phases and sizes of the particles. During the decomposition of these metal ion containing precursors, nascent metal oxides forms, which are basically small atomic clusters with proper chemical homogeneity, embedded in this porous carbonaceous material. These nascent metal oxides finally produce the desired phase of Fe_2O_3 nanopowders. The decomposition of carbonaceous material produces gases (such as CO, CO_2, NO_X, and water vapor) that help the precursor material to dissipate the heat of combustion and thus inhibit the sintering of fine particles during the process to produce nanosized oxides.[27,28]

TABLE I. Maghemite and hematite amount (in wt. %) and particle size of each phase for the obtained samples by modified sol-gel method.

Sample	α-Fe_2O_3 (wt. %)	Average size of particles in α-Fe_2O_3 phase (nm)	γ-Fe_2O_3 (wt. %)	Average size of particles in γ-Fe_2O_3 phase (nm)
A6	53	53	47	31
A 12	22	50	78	17
A 18	0	…	100	15
A 24	5	37	95	17

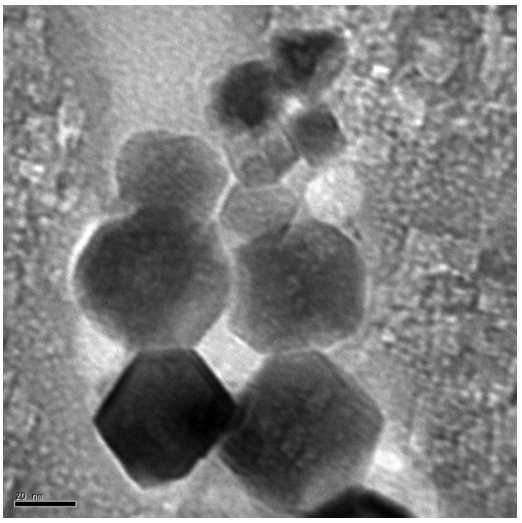

FIG. 3. TEM micrographs of the A6 sample presenting two different morphologies (JEOL JEM-1400 at 120 kV).

Average particle size of the obtained iron oxide powders was measured by TEM. The micrographs for the samples A6 and A18 are shown in Figures 3 and 4. It can be observed that A6 sample presents two crystalline phases, with different morphologies, hexagonal and cubic corresponding to hematite and maghemite phase, respectively. Average sizes observed by TEM micrographs for A6 sample are in agreement with the results obtained by Scherrer's equation, in the range of 50 nm for hematite phase and 30 nm for maghemite phase. It can be observed that A18 sample is composed by cubic particles with average size of 15 nm, also in agreement with the results obtained by Scherrer's equation.

Intending to study the optical properties (such as absorption and optical band gap energy) of the obtained iron oxides (hematite and maghemite are n type semiconductors), the photoacoustic UV-Vis spectra for A6 and A18 samples (Figure 5) were measured. In both cases, a broad absorption was registered near the 280–550 nm range of the spectrum.

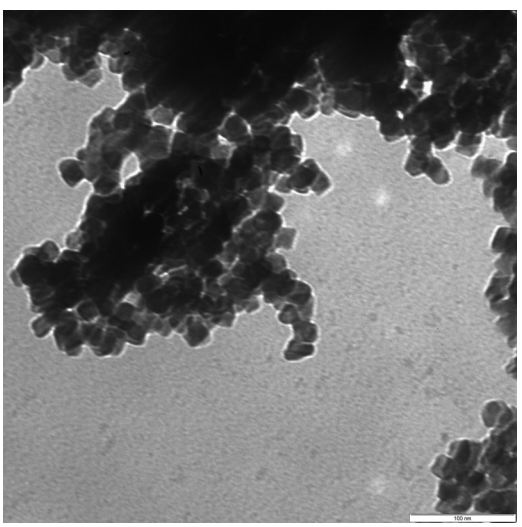

FIG. 4. TEM micrographs of the A18 sample, composed by cubic particles of 15 nm of average size (Zeiss EM10 at 80 kV).

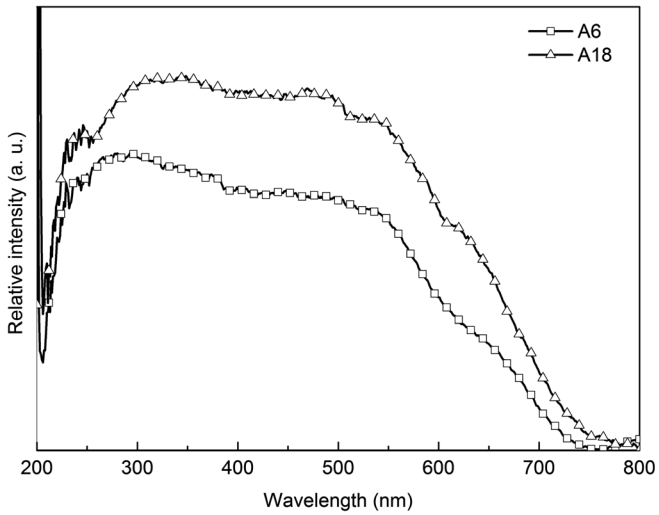

FIG. 5. Photoacoustic UV-Vis spectra of A6 and A18 samples.

These spectra reflect structural and other properties of the materials. They are the result of three types of electronic transitions: (i) Fe^{III} crystal or ligand field transitions, (ii) interactions between magnetically coupled Fe^{III} ions, and (iii) ligand (oxygen)-metal charge transfer excitations from the O(2p) non-bonding valence bands to the Fe(3d) ligand field orbitals. The charge transfer transitions involving Fe^{III}-O are mainly responsible for absorption of visible light. The electronic transitions $^4A_1 \leftarrow {}^6A$, d-d eletron pair transition, and $^4T_2 \leftarrow {}^6A_1$ present the respective band positions range in 420–440 nm, 520–570 nm, and 670–700 nm for hematite and 420–430 nm, 490–500 nm and 650–700 nm for maghemite.[19]

From the photoacoustic spectra data, the band gap energy were calculated (Figure 6), according to solid band theory, using the Tauc's equation[29]

$$(\alpha h\nu) = A(h\nu - E_g)^m, \tag{2}$$

where α is the absorption coefficient, A is a constant related to the effective mass of the electrons and holes, m is 0.5 for allowed direct transition, 2 for allowed indirect transitions, and E_g is the energy gap. A direct band gap follows the law: $(\alpha h\nu)^2 = A(h\nu - E_g)$, so if there is a direct band gap, a plot of $(\alpha h\nu)^2$ versus $h\nu$ would have a linear region with slope A and whose extrapolation to $\alpha(h\nu) = 0$ would give the value of E_g. On the other hand, data from indirect band gaps meet usually the Tauc law: $(\alpha h\nu)^{1/2} = B_{Tauc}(h\nu - E_g)$, where B_{Tauc} (Tauc parameter) is the slope of the linear region in a plot of $(\alpha h\nu)^{1/2}$ versus hν, whose extrapolation to $\alpha(h\nu) = 0$ would give the value of the indirect band gap[30] (Figure 6). The band gap values were found to be approximately the same for both samples, exhibiting an indirect transition at nearly 1.54 eV and direct transition at 1.77 and 1.91 eV, respectively, for A6 and A18 samples. Higher values of direct band gap have already been reported in the literature for bulk or nanoparticle iron oxides (2.84 eV for low-dimension nanoparticles and 2.2 eV for both bulk hematite, 30 nm Fe_2O_3 and 8 nm Fe_2O_3).[31,32] It is possible that the energy gap is influenced by size of the obtained iron oxide nanoparticles as well as the presence of two different crystalline phases, since most of the researches reports only band gap energies for hematite phase of iron oxide, and in this case, the samples present also a fraction of maghemite phase.[33] The indirect transition has been identified as a spin-forbidden Fe^{3+} 3d→3d excitation while the direct transition corresponds to the O^{2-} 2p→Fe^{3+} 3d charge transfer.[34,35]

The magnetization curves for all samples (Figure 7) were measured as a function of temperature (5–300 K), for an applied magnetic field of 500 Oe, using zero-field-cooling (ZFC) and field-cooling (FC) procedures. In the ZFC measurements, the samples were cooled down, from 300 K to 5 K, without the presence of an applied magnetic field. After reach 5 K, the magnetic field was applied, and the magnetization was measured during the temperature run. In the FC measurements, the samples were cooled down to 5 K with the same magnetic field applied during the ZFC. After reach 5 K, the magnetization was acquired during the temperature run.

All the ZFC-FC curves (Fig. 7) show irreversibility below T_{irr} (temperature below which the ZFC and FC curves are separated), and these temperatures are found to be $T_{irr} \sim 297$ K for the all samples. This behavior is typical of

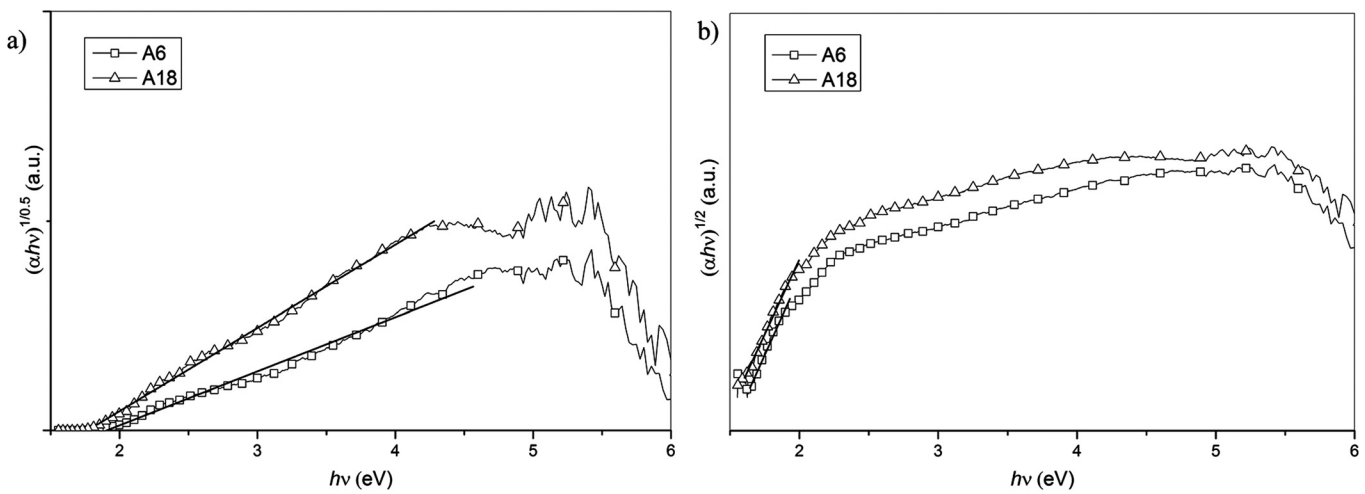

FIG. 6. Determination of E_g from Tauc's equation for (a) direct transitions (m = 0.5) and (b) indirect transitions (m = 2). The curves in bold line are the extrapolation of the Tauc's equation.

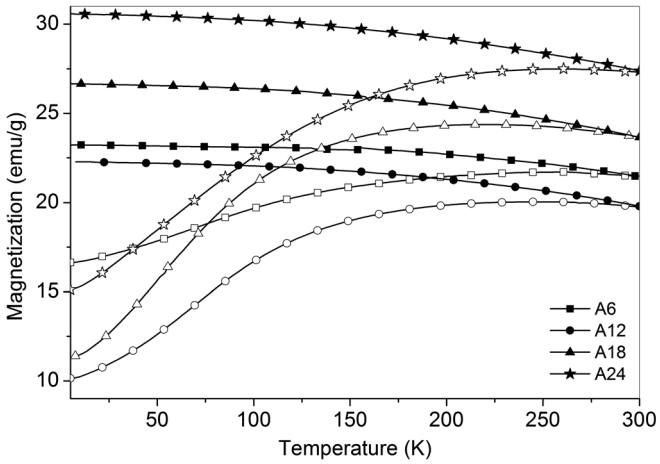

FIG. 7. ZFC (open symbols) and FC (solid symbols) magnetization curves of A6, A12, A18, and A24 samples at H = 500 Oe.

the blocking process for an assembly of superparamagnetic nanoparticles. A broad peak below room temperature can be viewed in the ZFC magnetization curves, with a maximum at T_{peak} ~258, 254, 215, 260 K for A6, A12, A18, and A24, respectively. As the maghemite particle size increases (for A6 and A12 samples), the T_{peak} shifts towards higher temperatures. This behavior is expected since bigger particles needs more thermal energy (KbT, where Kb is the Boltzmann constant and T is the absolute temperature) to overcome the potential barrier (KV, where K is the magnetic anisotropy and V is the particle volume). In the case of the sample A24, interactions between the alpha and gamma phases change the average anisotropy constant (K) into an effective one (K_{eff}) that modifies the blocking temperature and the spin-lattice relaxation time.[36]

In order to study the behaviour of the Fe_2O_3 nanoparticles above room temperature, the magnetization was recorded during the temperature run (5 K/min) for an applied magnetic field of 10 kOe (Figure 8).

All samples behave on the same way, and for clarity, only the changes in magnetization of the samples A6 and

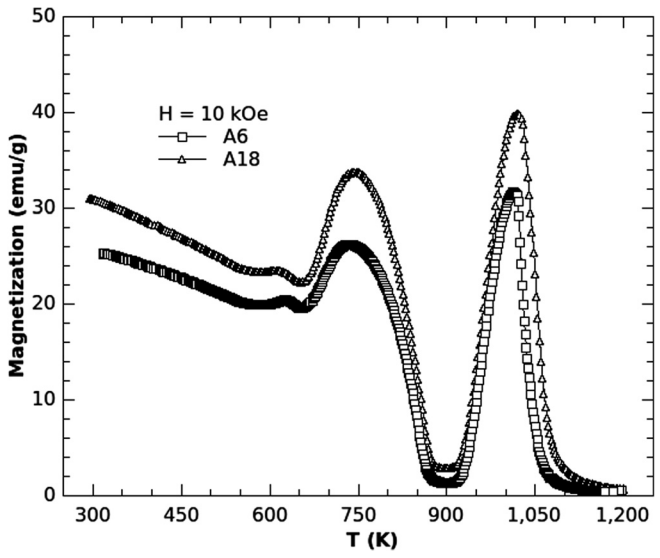

FIG. 8. Dependence of magnetization on temperature in a magnetic field of 10 kOe.

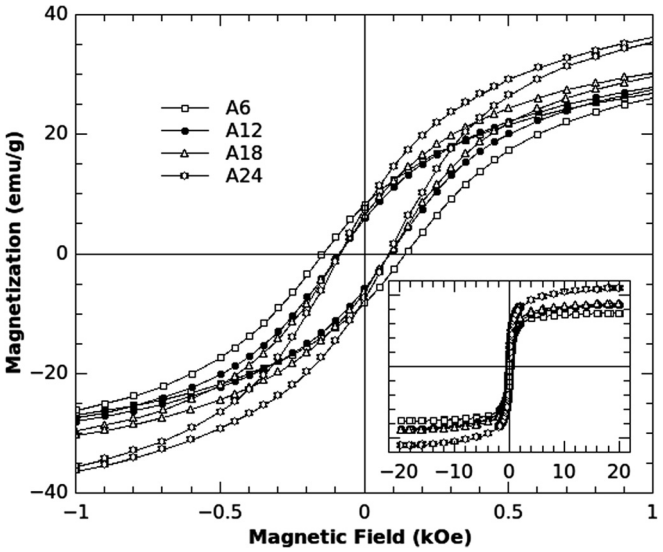

FIG. 9. Room-temperature magnetization vs magnetic applied field curves.

A18 are presented. As can be seen, there are two strong increases in magnetization. The first one that begins at ~650 K and reaches a maximum at ~745 K is related with the maghemite-hematite phase transition (MHPT). Many factors can influence on the MHPT temperature, e.g., maghemite particle size, heating rate, preparation method, etc. For nanoparticles, one can find this transition temperature ranging from 470 to 770 K, whereas for bulk samples, the range is 770–870 K.[37] After the MHPT a decay in magnetization is expected since the ferromagnetic maghemite turns into an antiferromagnetic hematite. The second and more defined

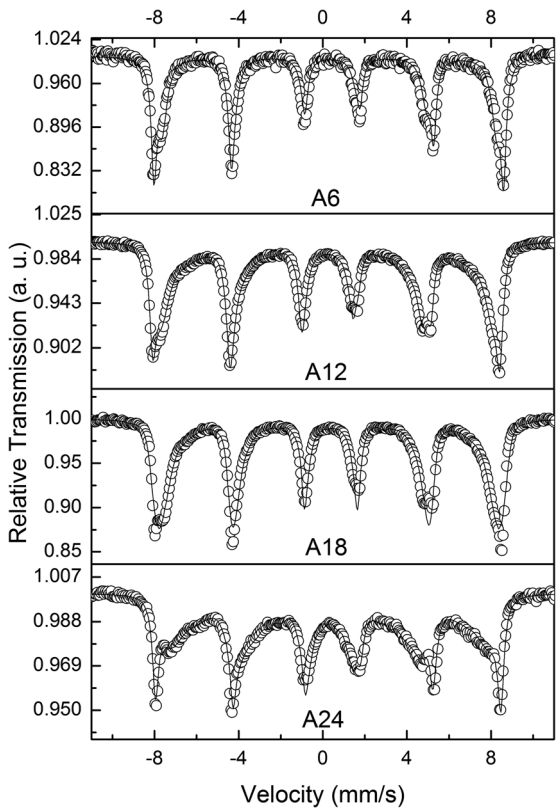

FIG. 10. Mossbauer spectra for A6, A12, A18, and A24 samples taken at room temperature.

TABLE II. Hyperfine parameters and subspectral areas for the obtained iron oxides.

Sample	Sub-espect.	Γ[a] (mm/s)	δ[b] (mm/s)	ΔE[c] (mm/s)	Bhf[d] (T)	A[e] (%)
A6	Distribution M	0.58	0.32	−0.02	49.3	56.9
	Sextet H	0.29	0.37	−0.18	51.5	43.1
A12	Distribution M	0.30	0.32	0.00	42.4	77.8
	Sextet H	0.33	0.38	−0.20	51.2	22.2
A18	Distribution M	0.30	0.34	−0.09	45.8	100
A24	Distribution M	0.30	0.33	0.03	35.5	76.5
	Sextet H	0.34	0.37	−0.23	50.9	23.5

[a]Γ: linewidth.
[b]δ: isomer shift.
[c]ΔE: quadrupole splitting.
[d]Bhf: hyperfine magnetic field.
[e]A: Area.

peak has a maximum at ∼1015 K and is related to the hematite Néel temperature.

The magnetization *versus* magnetic field curves, performed at room temperature, are shown in Figure 9.

The maximum applied field of 20 kOe was sufficient to saturate all the samples that presented the same trend on the curves. As can be seen from the inset in Figure 9, the highest magnetization saturation (55.1 emu/g) was achieved by the sample A24 (5 wt. % hematite and 95 wt. % maghemite), against 44.3 emu/g of the sample A18 (100 wt. % maghemite).

This can be explained by the presence of defects in the hematite nanoparticles caused by oxygen vacancies near the surface.[38] These defects could destroy the antiferromagnetic superexchange interaction of the Fe^{3+}-O^{2-}-Fe^{3+} leading to a ferromagnetic ordering.[39] Moreover, it is very difficult to determine exactly the saturation magnetization value without a large error bar. This limitation comes from the undetermined non-magnetic contributions to the measured mass needed to calculate the sample magnetization.

Figure 10 shows the room-temperature transmission Mossbauer spectra of the samples A6, A12, A18, and A24. Table II gives the results of the spectra fitting. The phases expected in the sample are γ-Fe_2O_3 and α-Fe_2O_3 as suggested by the XRD results.

γ-Fe_2O_3 has the spinel structure where the cation distribution can be described by the formula $Fe^{3+}[\square Fe^{3+}]O_3$, with cations without brackets are on tetrahedral A-sites and those in brackets are on octahedral B-sites of the cubic spinel lattice. The symbol □ represents the vacante B-sites in γ-Fe_2O_3. There is only one crystalline lattice site for Fe^{3+} in hexagonal α-Fe_2O_3.[40] At room temperature, hematite spectrum consists of a sextet with a ΔE of $-0.20\,mm\,s^{-1}$, a B_{hf} of 51.8 T, and δ of $0.38\,mm\,s^{-1}$.[19,41] The spectrum of maghemite is composed of two sextets, hardly distinguishable at room temperature, due to the fact that hyperfine parameters for the two sites are very similar in magnitude. Commonly occurring effects such as small particle size distributions tend to cause line broadening and/or a line-shape asymmetry, and in many cases the room temperature spectrum has to be fit with a distribution of unresolved A- and B-site hyperfine fields.[42] This fact occurs in this work, where the maghemite phase was fitted as distribution M. In surveying the literature for maghemite it was noticed that an inconceivably wide scatter for the δ exists, with the values at room temperature ranging from $0.04\,mm\,s^{-1}$ up to $0.30\,mm\,s^{-1}$ for A-site and from $0.04\,mm\,s^{-1}$ up to $0.40\,mm\,s^{-1}$ for B-site, and B_{hf} values for the two sites were 50.0 T.[19,42] The spectra for all samples were adjusted by introducing one sextet relative to hematite and a distribution relative to maghemite. It can be observed that the Mossbauer spectra of hematite and maghemite overlap at room temperature, so it is difficult to quantify the relative proportions of these phases in the samples. Due to this, there may be slight difference between the proportions of crystalline phases (α-Fe_2O_3 and γ-Fe_2O_3) determined by Mössbauer spectroscopy and Rietveld refinement.

IV. CONCLUSIONS

Nanosized iron oxide particles have been synthesized by the modified sol-gel method. Analysis of XRD patterns showed that the samples have maghemite or hematite+maghemite phases. There is a tendency of the average particle size of the iron oxide samples to decrease as the amount of PVA used in the synthesis increases. On the other hand, one of the intermediate Fe^{3+}:PVA monomeric unit ratio used in the synthesis (1:18) allowed pure maghemite preparation. For this sample (A18), XRD and TEM results lead to an average size of 15 nm. The saturation magnetization increases, increasing the amount of PVA in the synthesis, and has a maximum of 55.1 emu/g for A24 sample. Mössbauer spectrum confirms the results obtained by x-ray diffraction, indicating the presence of maghemite and hematite phases. The superparamagnetic behavior of the nanoparticles below Tpeak was confirmed by ZFC-FC measurements. Maghemite-hematite transition phase and hematite Néel transition were determined by magnetization at higher temperature as ∼700 K and 1015 K, respectively.

ACKNOWLEDGMENTS

The authors would like to thank Professor Dr. Mauro Baesso and Ms. Gutierrez Rodriguês de Morais for UV-Vis photoacoustic measurements and Professor Dr. Eduardo Radovanovic and David Garcia Ros for TEM micrographs. The authors thank the financial support of Capes—DGU 184-09 and MCI Spain—PHB 2008-0044-PC.

[1]P. Xu, G. M. Zeng, D. L. Huang, C. L. Feng, S. Hu, M. H. Zhao, C. Lai, Z. Wei, C. Huang, G. X. Xiea, and Z. F. Liu, Sci. Total Environ. **424**, 1–10 (2012).
[2]F. Rajabi, N. Karimi, M. R. Saidi, A. Primo, R. S. Varma, and R. Luque, Adv. Synth. Catal. **354**, 1707–1711 (2012).
[3]H. Kitamuraa, L. Zhaob, B. T. Hangc, S. Okadab, and J.-i. Yamaki, J. Power Sources **208**, 391–396 (2012).
[4]A. Figuerola, R. Di Corato, L. Manna, and T. Pellegrino, Pharmacol. Res. **62**, 126–143 (2010).
[5]H.-M. Yang, B. C. Oh, J. H. Kim, T. Ahn, H.-S. Nam, C. W. Park, and J.-D. Kim, Colloids Surf., A **391**, 208–215 (2011).
[6]H. Xu, Z. P. Aguilar, L. Yang, M. Kuang, H. Duan, Y. Xiong, H. Wei, and A. Wang, Biomaterials **32**, 9758–9765 (2011).
[7]M. Mahmoudi, S. Sant, B. Wang, S. Laurent, and T. Sen, Adv. Drug Delivery Rev. **63**, 24–46 (2011).
[8]J.-P. Jolivet, S. Cassaignon, C. Chanéac, D. Chiche, O. Durupthy, and D. Portehault, C. R. Chim. **13**, 40–51 (2010).
[9]S. Yang, Y.-H. Jang, C. H. Kim, C. Hwang, J. Lee, S. Chae, S. Jung, and M. Choi, Powder Technol. **197**, 170–176 (2010).
[10]Y. Wu and X. Wang, Mater. Lett. **65**, 2062–2065 (2011).
[11]D. M. Fernandes, A. A. W. Hechenleitner, M. F. Silva, M. K. Lima, P. R. S. Bittencourt, R. Silva, M. A. C. Melo, and E. A. G. Pineda, Mater. Chem. Phys. **118**, 447–452 (2009).
[12]L.-H. Han, H. Liu, and Y. Wei, Powder Technol. **207**, 42–46 (2011).
[13]L. Chen, Z. Lin, C. Zhao, Y. Zheng, Y. Zhou, and H. Peng, J. Alloy Compd. **509**, L1–L5 (2011).
[14]A. Hassanjani-Roshan, M. R. Vaezi, A. Shokuhfar, and Z. Rajabali, Particuology **9**, 95–99 (2011).
[15]A. Khaleel and A. Al-Marzouqi, Mater. Lett. **68**, 385–387 (2012).
[16]S. Komarneni, W. Hu, Y. D. Noh, A. V. Orden, S. Feng, C. Wei, H. Pang, F. Gao, Q. Lu, and H. Katsuki, Ceram. Int. **38**, 2563–2568 (2012).
[17]D. M. Fernandes, R. Silva, A. A. W. Hechenleitner, E. Radovanovic, M. A. C. Melo, and E. A. G. Pineda, Mater. Chem. Phys. **115**, 110–115 (2009).
[18]J. Rodriguez-Carvajal, Physica B **192**, 55–69 (1993).
[19]R. M. Cornell and U. Sshwertmann, *The Iron Oxides: Structures, Properties, Reactions, Occurrences and Uses* (John Wiley & Sons, 2003).
[20]M. Gotic and S. Music, J. Mol. Struct. **834–836**, 445–453 (2007).
[21]D. Predoi, Dig. J. Nanomater. Biostruct. **2**, 169–173 (2007).
[22]H. Namduri and S. Nasrazadani, Corros. Sci. **50**, 2493–2497 (2008).
[23]M. A. Gulgun, M. H. Nguyen, and W. M. Kriven, J. Am. Ceram. Soc. **82**, 556–560 (1999).
[24]J. Feng, T. Liu, Y. Xu, J. Zhao, and Y. He, Ceram. Int. **37**, 1203–1207 (2011).
[25]G. C. P. Tae-Jin Park, A. R. Moodenbaugh, Y. Mao, and S. S. Wong, J. Mater. Chem. **15**, 2099–2105 (2005).
[26]T. Liu, Y. Xu, and J. Zhao, J. Am. Ceram. Soc. **93**, 3637–3641 (2010).
[27]P. P. Sarangi, B. Naik, and N. N. Ghosh, Powder Technol. **192**, 245–249 (2009).
[28]P. P. Sarangi, B. D. Naik, S. R. Vadera, M. K. Patra, C. Prakash, and N. N. Ghosh, Mater. Technol.: Adv. Perform. Mater. **24**, 97–99 (2009).
[29]J. Tauc, R. Grigorovici, and A. Vancu, Phys. Status Solidi **15**, 627 (1966).
[30]F. L. Martínez, M. Toledano-Luque, J. J. Gandía, J. Cárabe, W. Bohne, J. Röhrich, E. Strub, and I. Mártil, J. Phys. D: Appl. Phys. **40**, 5256 (2007).
[31]M. M. Rahman, S. B. Khan, M. Faisal, A. M. Asiri, and M. A. Tariq, Electrochim. Acta **75**, 164–170 (2012).
[32]B. Gilbert, C. Frandsen, E. R. Maxey, and D. M. Sherman, Phys. Rev. B **79**, 035108 (2009).
[33]T. Echigo, D. M. Aruguete, M. Murayamac, and M. F. Hochella, Jr., Geochim. Cosmochim. Acta **90**, 149–162 (2012).
[34]A. Duret and M. Gratzel, J. Phys. Chem. B **109**, 17184–17191 (2005).
[35]F. L. Souza, K. P. Lopes, P. A. P. Nascente, and E. R. Leite, Sol. Energy Mater. Sol. Cells **93**, 362–368 (2009).
[36]L. A. S. de Oliveira, J. P. Sinnecker, M. D. Vieira, and A. Penton-Madrigal, J. Appl. Phys. **107**, 09D907 (2010).
[37]G. Ennas, G. Marongiu, A. Musinu, A. Falqui, P. Ballirano, and R. Caminiti, J. Mater. Res. **14**, 1570–1575 (1999).
[38]J. Wu, S. Mao, Z. Ye, Z. Xie, and L. Zheng, ACS Appl. Mater. Interfaces **2**, 1561–1564 (2010).
[39]N. D. Phu, D. T. Ngo, L. H. Hoang, N. H. Luong, N. Chau, and N. H. Hai, J. Phys. D: Appl. Phys. **44**, 345002 (2011).
[40]H. Nagar, N. V. Kulkarni, S. Karmakar, B. Sahoo, I. Banerjee, P. S. Chaudhari, R. Pasricha, A. K. Das, S. V. Bhoraskar, S. K. Date, and W. Keune, Mater. Charact. **59**, 1215–1220 (2008).
[41]A. T. Goulart and M. F. d. J. Filho, Hyperfine Interact. **83**, 451–455 (1994).
[42]G. M. Costa, E. Grave, L. H. Bowen, R. E. Vandenberghe, and P. M. A. Bakker, Clay Clay Miner. **42**, 628–633 (1994).